nature photonics

SUPPLEMENTARY INFORMATION

https://doi.org/10.1038/s41566-019-0576-2

In the format provided by the authors and unedited.

Snapshot photoacoustic topography through an ergodic relay for high-throughput imaging of optical absorption

Yang Li[1,2,6], Lei Li[1,6], Liren Zhu[1,2,6], Konstantin Maslov[1], Junhui Shi[1], Peng Hu[1], En Bo[1], Junjie Yao[2,3], Jinyang Liang[1,4], Lidai Wang[2,5] and Lihong V. Wang[1]*

[1]Caltech Optical Imaging Laboratory, Andrew and Peggy Cherng Department of Medical Engineering, Department of Electrical Engineering, California Institute of Technology, Pasadena, CA, USA. [2]Department of Biomedical Engineering, Washington University in St. Louis, St. Louis, MO, USA. [3]Present address: Duke Photoacoustic Imaging Laboratory, Department of Biomedical Engineering, Duke University, Durham, NC, USA. [4]Present address: Laboratory of Applied Computational Imaging, Institut National de la Recherche Scientifique, Varennes, Quebec, Canada. [5]Present address: Department of Mechanical and Biomedical Engineering, City University of Hong Kong, Kowloon Tong, Hong Kong, China. [6]These authors contributed equally: Yang Li, Lei Li, Liren Zhu. *e-mail: LVW@caltech.edu

Snapshot Photoacoustic Topography Through an Ergodic Relay for High-throughput Imaging of Optical Absorption

Yang Li[1,2†], Lei Li[2,3†], Liren Zhu[1,2†], Konstantin Maslov[2], Junhui Shi[2], Peng Hu[1,2], En Bo[2], Junjie Yao[1‡], Jinyang Liang[1,2‡], Lidai Wang[1‡], and Lihong V. Wang[2,3*]

Supplementary Materials

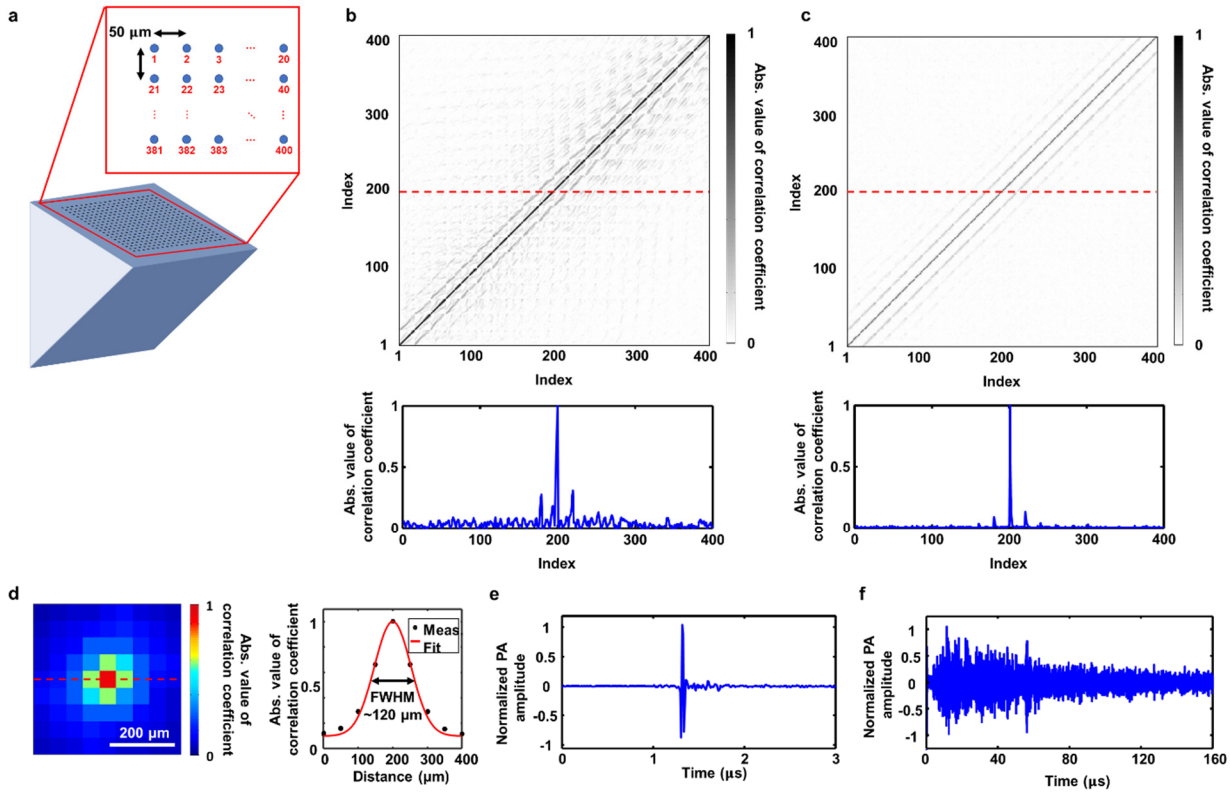

Supplementary Figure 1. Characterization of the prism as an ergodic relay. (a) Schematic demonstrating 400 pixels on the illumination face of the ER prism. The pixels were sampled from a square region on the illumination face of the prism with 20-by-20 steps and a 50 µm step size. The red box represents a zoomed-in view of the pixels. The numbers in red are the indices to the pixels. (b) Cross-correlation map of the encoded PA signals from the pixels, where the diagonal line represents autocorrelation (top). Line profile along the red dashed line (bottom). (c) Cross-correlation map of the encoded PA signals that are truncated to remove the first-arrival signals (i.e., signals propagating directly from the sources to the ultrasonic transducer without scrambling inside the ergodic relay), showing the time traces of the sufficiently encoded PA signals are almost orthogonal to each other (top). Line profile along the red dashed line (bottom). (d) Averaged cross-correlation map of the reshaped and co-registered maps from (b) (top) and the profile along the

red dashed line (bottom). The full width at half maximum (FWHM) of the fitted profile is ~120 μm. Abs., absolute. Meas., measurement. (e) A-line signal from a point source detected using a conventional OR-PAM system. The significant portion of the signal lasted approximately 100 ns. (f) Encoded impulse response from a point source recorded using PATER for 164 μs.

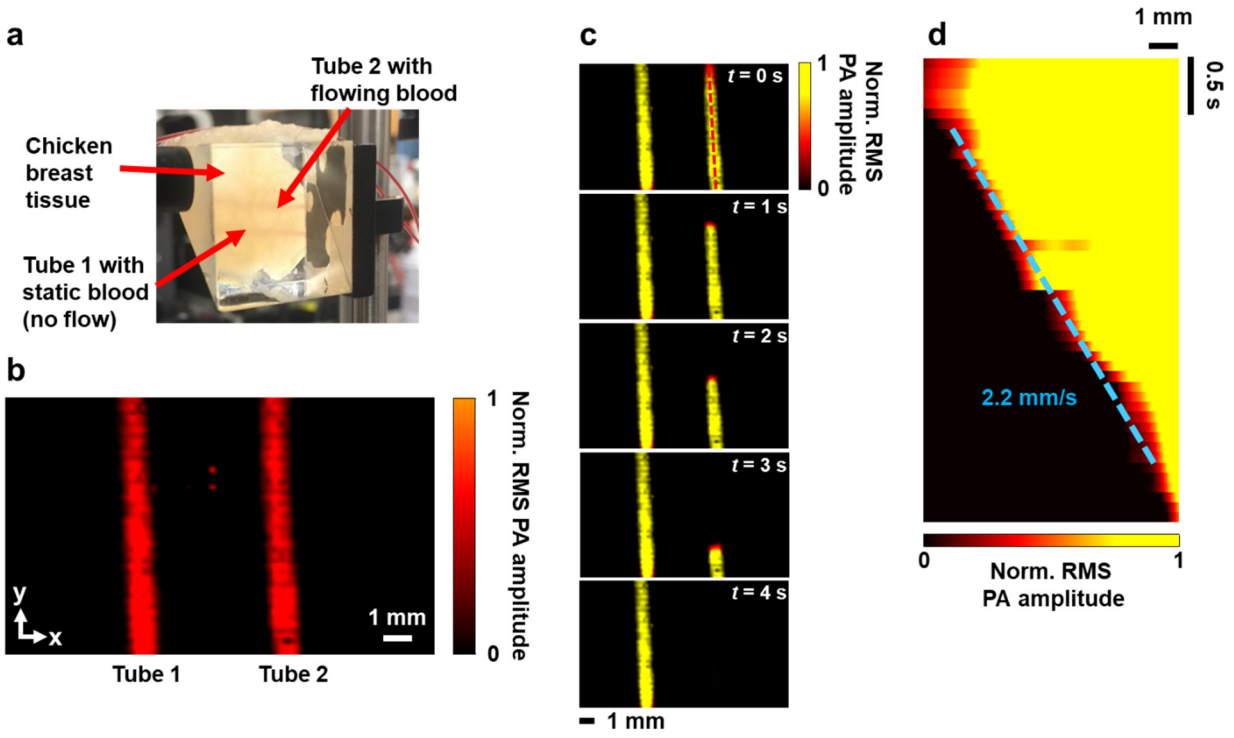

Supplementary Figure 2. PATER imaging of blood flow behind scattering biological tissue. (a) Photograph of the imaged object. A layer of chicken breast tissue (~1 mm thickness) was used as the scattering medium. Two tubes filled with blood were placed behind the tissue. While Tube 1 served as the control without flow, blood flowed through Tube 2. (b) Calibration image of the two tubes. Norm., normalized. (c) Widefield images of blood flushing out of Tube 2 (from top to bottom) acquired at various time points. (d) Space-time domain plot of pixels along the red dashed line in (c). The blue dashed line and label show the approximated flow speed of blood through the tube.

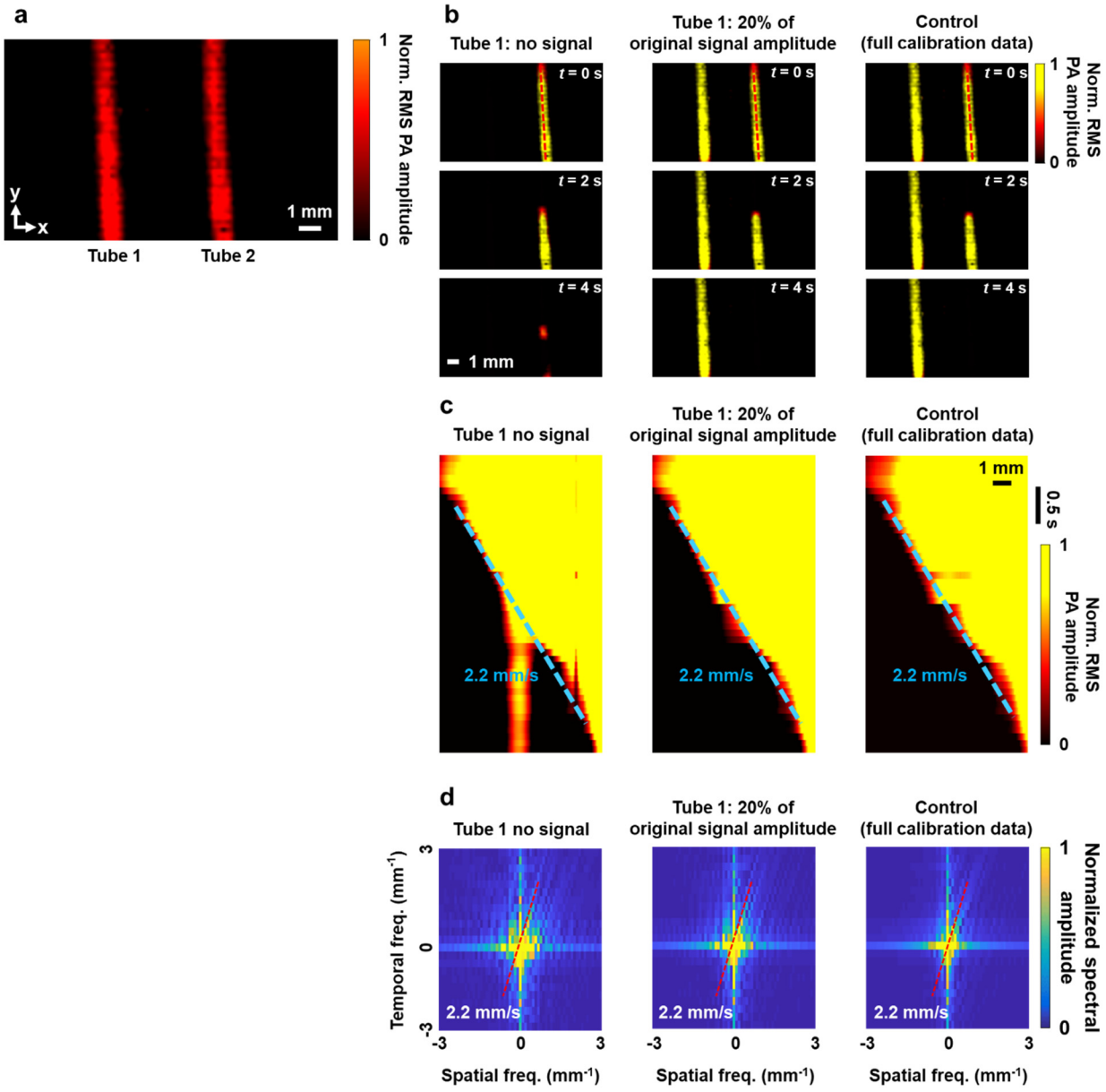

Supplementary Figure 3. Evaluation of reconstruction artefacts due to incomplete calibration. (a) Calibration image of the two tubes. Norm., normalized. (b) Comparison of partial-signal and full-signal reconstructions. In the partial-signal cases, the amplitude of the calibration signal from Tube 1 was manually suppressed to simulate conditions in which there were not enough blood signals in Tube 1 during calibration (no signal, and only 20% of original signal amplitude). The widefield

signals from both tubes were used to test each case of the calibration data. The results are compared with the control case, in which full calibration data from Tube 1 was used for calibration. (c) Space-time domain plot of pixels along the axis of Tube 2 in the different cases in (b). The artefacts due to incomplete calibration are absent, even with only 20% of the original signal amplitude from Tube 1. The blue dashed lines and labels show the flow speeds of blood through the tube. (d) 2D Fourier transform images of (c). The slopes of the red dashed lines represent the flow speeds, which were approximately 2.2 mm/s for all three cases. The partial-signal reconstructions and analyses show that blood flow dynamics in Tube 2 can be accurately reconstructed even if widefield signals from Tube 1 appear after calibration.

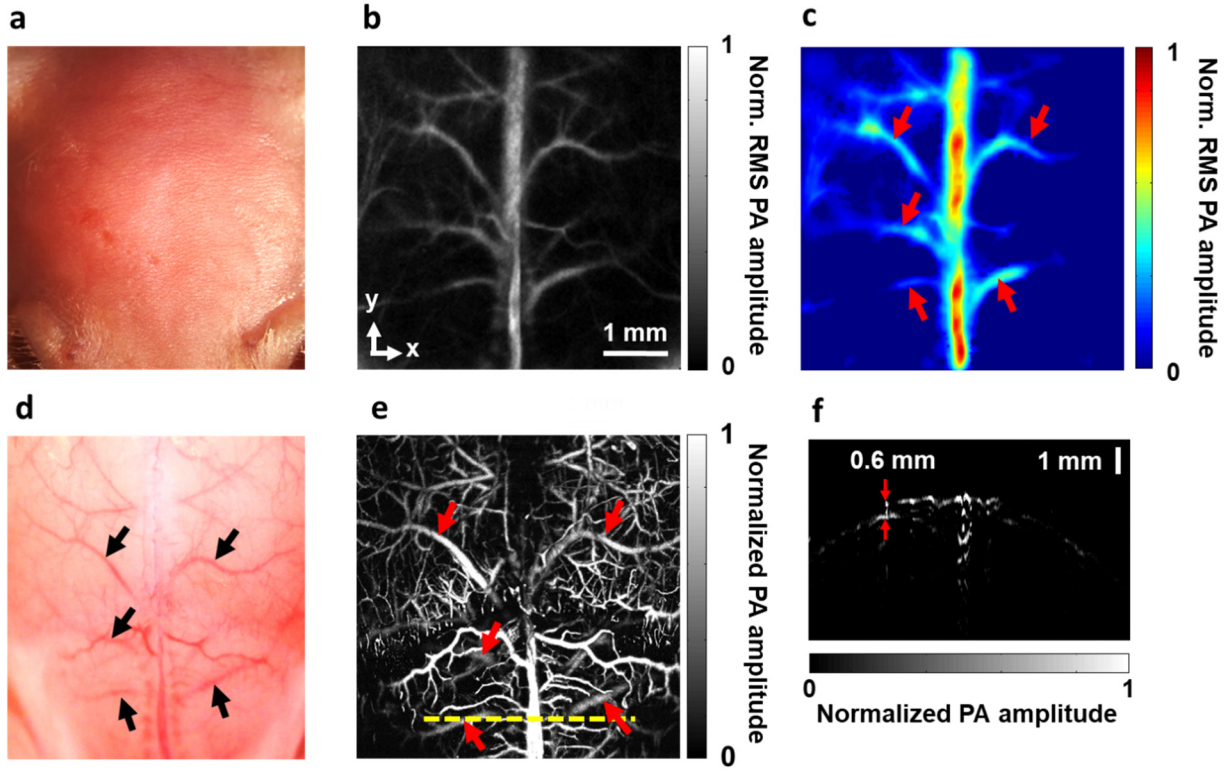

Supplementary Figure 4. PATER imaging of deep mouse brain through intact scalp ($N = 3$). (a) Photograph of the mouse brain with hair removed. (b) Calibration image of the mouse brain vasculature through an intact scalp and skull. (c) Snapshot widefield image of the mouse brain vasculature acquired through an intact scalp. (d) Photograph of the mouse brain vasculature with the scalp removed, acquired after the PATER imaging. (e) Maximum amplitude projection image of the mouse brain vasculature acquired without scalp by conventional optical-resolution PAM. (f) B-scan image below the dashed line in Panel e. The deepest vessel shown in Panel c along the same line was approximately 0.6 mm below the bottom surface of the skull. Since the thickness of the scalp was ~0.3 mm and the thickness of the skull was ~0.2 mm, the total depth from the ergodic relay input surface to the vessel was ~1.1 mm.

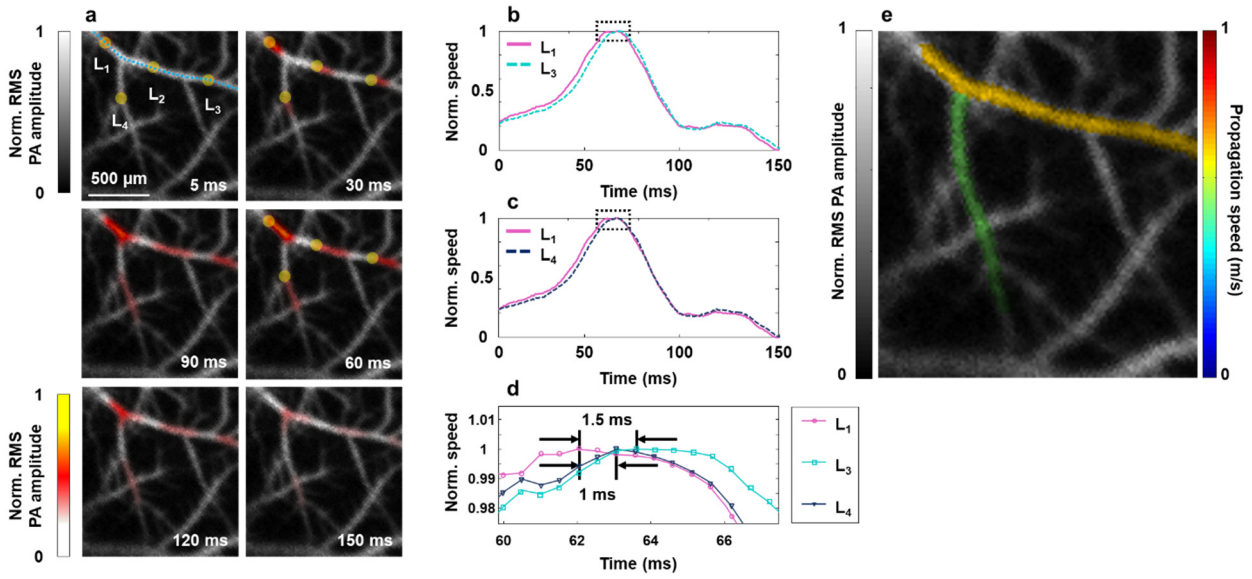

Supplementary Figure 5. Mapping of pulse wave velocity (PWV) by imaging the blood flow at multiple sites simultaneously. (a) Widefield images showing thermal wave propagation in the mouse middle cerebral arteries. The yellow circles, labelled L_1–L_4, indicate locations of the laser heating spots during recording. (b) Plot of averaged blood flow speeds at spots L_1 and L_3. (c) Plot of averaged blood flow speeds at spots L_1 and L_4. (d) Zoomed-in view of the peaks shown in the dotted boxes in (b) and (c). (e) Map of PWV at two branches of the middle cerebral arteries. The vessel diameter of each branch was assumed to be constant.

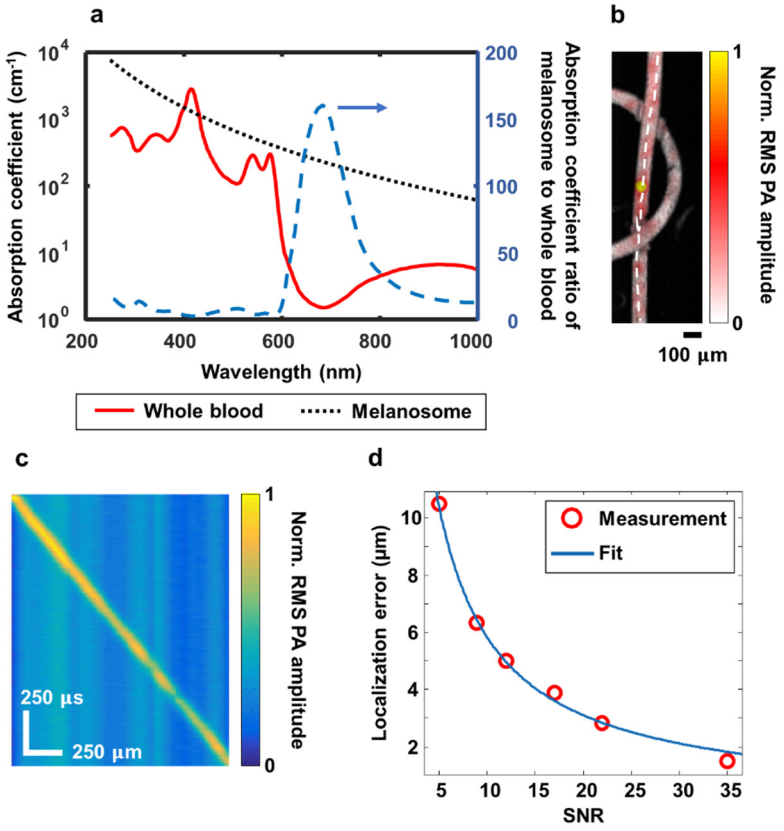

Supplementary Figure 6. Phantom study of melanoma tumour cells (MTCs). (a) Absorption spectra of whole blood (85% oxygen) and melanosome. (b) PATER imaging of MTCs flowing through a tube (120 µm in diameter) filled with blood. The MTCs and the blood are driven through the tube by a syringe pump. (c) Space-time domain plot of PA signals along the dashed line in (b). The slope from the plot was computed by linear fitting to be ~1 mm/s, which was the flow speed of the MTCs. (d) Plot of localization error at different signal-to-noise ratios (SNRs). MTC clusters with different concentrations were prepared by mixing agar with blood and MTCs. The clusters were then injected into the tube shown in (b) and driven by a syringe pump to flow through the tube. The computed localization errors at different SNRs were fitted with the function $f(\mathrm{SNR}) = a/\mathrm{SNR}$, where a is a constant. The fitting shows that the localization error is inversely proportional to the value of SNR.

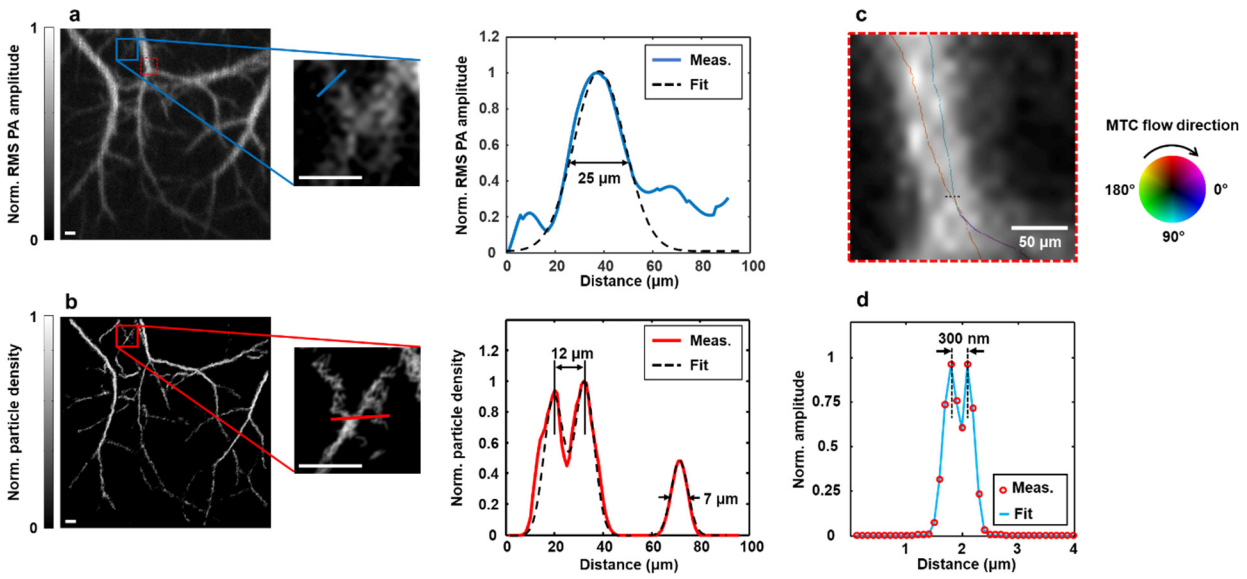

Supplementary Figure 7. Quantification of spatial resolution in the localization map of mouse brain. (a) Calibration image of the mouse brain and a zoomed-in view of the blue boxed region showing a group of small vessels. The plot shows the profile along the blue line in the zoomed-in view and a Gaussian fit calculated using MATLAB's curve-fit toolbox. Meas., measurement. (b) Localization map of the mouse brain and a zoomed-in view of the red boxed region showing the same region as the blue boxed region in (a). The plot shows the profile along the red line in the zoomed-in view and a three-term Gaussian fit. The two neighboring vessels branching out from each other can be separated at a distance of 12 µm, and the FWHM for the small vessel is 7 µm. Scale bars in (a) and (b), 100 µm. (c) Two summed localization traces of tumour cells migrating through two crossed blood vessels, superimposed on the red-boxed region in (a). A 25-time spatial running averaging was performed for each image to enhance the SNR. The colour indicates MTC flow direction inside the blood vessels. (d) Line profile across the grey dotted line in (c) at a distance of 300 nm.

Supplementary Note 1. Derivation of the noise-limited localization error.

For simplicity, the analysis is given in one dimension. The goal is to estimate the centre of the tracked particle, x_0, from the acquired PA amplitude, P_i, where i is the pixel index along the x axis. We assume a Gaussian PSF to represent the PA amplitude density with a dimension of amplitude per unit length:

$$p(x, x_0) = \frac{P}{\sqrt{2\pi}\sigma} \exp\left(-\frac{(x - x_0)^2}{2\sigma^2}\right), \tag{1}$$

where P is the PA amplitude and σ is the standard deviation (**Supplementary Fig. 8**). We use the least-squares fitting to evaluate x_0. The sum of the squared residuals is given by

$$\chi^2(x_0) = \sum \left(\frac{P_i}{l} - p(x_i, x_0)\right)^2, \tag{2}$$

where l is the width of a pixel, which is assumed to be much smaller than σ. Parameter x_0 is estimated by minimizing the sum:

$$\hat{x}_0 = \arg\min_{x_0} \chi^2(x_0). \tag{3}$$

The minimization is achieved by solving the following equation:

$$\frac{d\chi^2}{d\hat{x}_0} = \sum 2\left(\frac{P_i}{l} - p(x_i, \hat{x}_0)\right)\frac{\partial p(x_i, \hat{x}_0)}{\partial \hat{x}_0} = 0. \tag{4}$$

The Taylor expansion is invoked to the first order:

$$p(x_i, \hat{x}_0) = p(x_i, x_0) + \frac{\partial p(x_i, x_0)}{\partial x_0}\Delta\hat{x}_0, \tag{5}$$

where $\Delta\hat{x}_0 = \hat{x}_0 - x_0$. For notation brevity, we denote $p_i' = \partial p(x_i, x_0)/\partial x_0$. Inserting Eq. (5) into Eq. (4) yields

$$\sum (P_i - l \cdot p(x_i, x_0) - l \cdot p_i' \cdot \Delta\hat{x}_0) \cdot p_i' = 0, \tag{6}$$

We denote the measurement error as $\Delta P_i = P_i - l \cdot p(x_i, x_0)$, which is inserted into Eq. (6) to yield

$$\Delta\hat{x}_0 = \frac{\sum \Delta P_i p_i'}{l \sum {p_i'}^2}. \tag{7}$$

Because the only random variable on the right-hand side of Eq. (7), ΔP_i, is an independent zero-mean Gaussian random variable, $\Delta\hat{x}_0$ must be a zero-mean Gaussian random variable as well. Therefore, the estimation is unbiased. By squaring Eq. (7) and calculating the expected value, we obtain the mean squared error as

$$\langle (\Delta\hat{x}_0)^2 \rangle = \frac{\langle (\sum \Delta P_i p_i')^2 \rangle}{l^2 \left(\sum {p_i'}^2\right)^2}. \tag{8}$$

Because ΔP_i at different indices are uncorrelated, $\langle (\sum \Delta P_i p_i')^2 \rangle = \sum {p_i'}^2 \langle (\Delta P_i)^2 \rangle$. Therefore, Eq. (8) becomes

$$\langle (\Delta\hat{x}_0)^2 \rangle = \frac{\sum {p_i'}^2 \langle (\Delta P_i)^2 \rangle}{l^2 \left(\sum {p_i'}^2\right)^2}. \tag{9}$$

We rewrite the expected noise power (not in absolute unit) as $\langle (\Delta P_i)^2 \rangle = N_l^2$, where N_l is the amplitude of the statistically stationary (that its statistical properties are independent of the index i) detector or environmental noise at pixel width l. Eq. (9) then becomes

$$\langle (\Delta\hat{x}_0)^2 \rangle = \frac{N_l^2}{l \sum l \cdot {p_i'}^2}. \tag{10}$$

We approximate the sum in the denominator in Eq. (10) with an integral:

$$\langle (\Delta\hat{x}_0)^2 \rangle = \frac{N_l^2}{l \int_{-\infty}^{+\infty} dx \left(\frac{\partial p(x, x_0)}{\partial x_0}\right)^2}, \tag{11}$$

where

$$\frac{\partial p(x, x_0)}{\partial x_0} = \frac{P}{\sqrt{2\pi}\sigma^3} (x - x_0) e^{-(x-x_0)^2/2\sigma^2}. \tag{12}$$

Therefore, it can be shown that

$$\langle(\Delta\hat{x}_0)^2\rangle = \frac{2\pi\sigma^6 N_l^2}{l\cdot P^2\int_{-\infty}^{+\infty} dx\,(x-x_0)^2 e^{-(x-x_0)^2/\sigma^2}}. \tag{13}$$

If we let $v = (x - x_0)$, we have

$$\langle(\Delta\hat{x}_0)^2\rangle = \frac{2\pi\sigma^6 N_l^2}{l\cdot P^2\int_{-\infty}^{+\infty} dv\,v^2 e^{-v^2/\sigma^2}}. \tag{14}$$

If we set a random variable $V\sim\mathcal{N}\left(0,\left(\frac{\sigma}{\sqrt{2}}\right)^2\right)$, whose probability density function is $\mathrm{pdf}(v) = \frac{1}{\sqrt{\pi}\sigma}e^{-v^2/\sigma^2}$, then Eq. (14) can be rearranged as follows:

$$\langle(\Delta\hat{x}_0)^2\rangle = \frac{2\pi\sigma^6 N_l^2}{l\cdot P^2\sqrt{\pi}\sigma\int_{-\infty}^{+\infty} dv\,v^2\frac{1}{\sqrt{\pi}\sigma}e^{-v^2/\sigma^2}}. \tag{15}$$

Since $\int_{-\infty}^{+\infty} dv\,v^2\frac{1}{\sqrt{\pi}\sigma}e^{-v^2/\sigma^2} = \int_{-\infty}^{+\infty} dv\,v^2\mathrm{pdf}(v) = E(V^2) = \mathrm{Var}(V) = \frac{\sigma^2}{2}$, Eq. (15) becomes

$$\langle(\Delta\hat{x}_0)^2\rangle = \frac{2\pi\sigma^6 N_l^2}{l\cdot P^2\sqrt{\pi}\sigma^3/2} = \frac{4\sqrt{\pi}\sigma^3 N_l^2}{l\cdot P^2}. \tag{16}$$

Denoting the maximum amplitude of the Gaussian PSF as $S_l = l\cdot\frac{P}{\sqrt{2\pi}\sigma}$, we convert Eq. (16) to

$$\langle(\Delta\hat{x}_0)^2\rangle = \frac{2l\sigma}{\sqrt{\pi}}\left(\frac{N_l}{S_l}\right)^2. \tag{17}$$

Next, we define an equivalent conceptual pixel of width $L = \sqrt{2\pi}\sigma$ centred at the peak of the PSF such that the area of the colored region shown in **Supplementary Fig. 8** is P. This pixel's associated signal and noise amplitudes are denoted as S_L and N_L, respectively. Since the signal amplitude is proportional to length, and the noise amplitude is proportional to the square root of length, we have $S_L/S_l = \frac{L}{l}$ and $N_L/N_l = \sqrt{\frac{L}{l}}$, which yield

$$\frac{N_l}{S_l} = \frac{N_L}{S_L}\sqrt{\frac{L}{l}}. \tag{18}$$

Substituting Eq. (18) into Eq. (17), we obtain

$$\langle(\Delta\hat{x}_0)^2\rangle = 2\sqrt{2}\sigma^2\frac{N_L^2}{S_L^2} = 2\sqrt{2}\sigma^2\cdot\frac{1}{\mathrm{SNR}_L^2}, \tag{19}$$

where the amplitude-based signal-to-noise ratio with a pixel width of L is defined as $\mathrm{SNR}_L = S_L/N_L$. Taking the square root of Eq. (19) leads to

$$\sqrt{\langle(\Delta\hat{x}_0)^2\rangle} = 2^{3/4}\frac{\sigma}{\mathrm{SNR}_L}. \tag{20}$$

In conclusion, the localization error is proportional to the original resolution of the system and inversely proportional to the value of SNR_L.

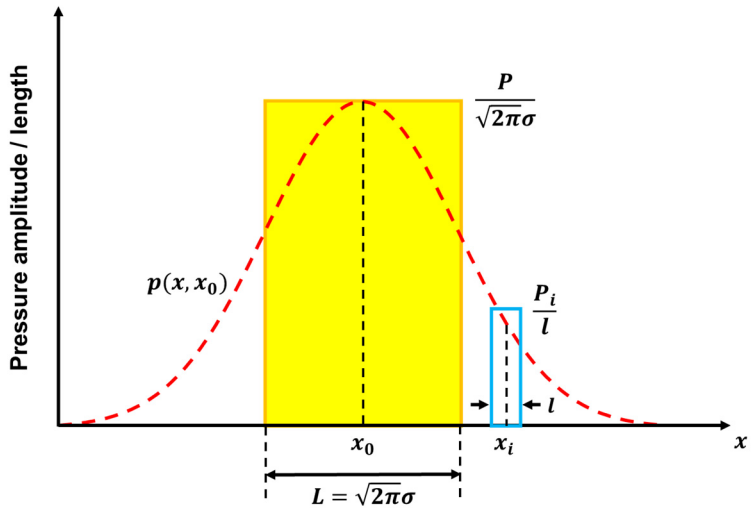

Supplementary Figure 8. Schematic representation of the least-squares fitting for the centre of a particle. P_i, measured PA amplitude of the particle at pixel of index i; $p(x, x_0)$, assumed Gaussian point-spread-function (PSF); x_0, the centre of the particle to be estimated; $x_i = i \cdot l$, the position of the ith pixel, where l is the pixel width. The coloured region represents an area of P for a conceptual pixel of width $L = \sqrt{2\pi}\sigma$.

Supplementary Note 2. Computation of the flow speed and direction of the MTCs.

We computed the flow speed and direction of the MTCs in each vessel by tracking them in real time and analyzing their movements. The computed flow speed of MTCs has a maximum of 0.54 mm/s, which is lower than the cerebral blood flow speed[1]. A velocity-contrast map is computed for the mouse cortical vasculature by analyzing the flow speed of MTCs in each vessel in the spatiotemporal frequency domain. Vessels in the mouse brain can be individually identified based on the differences in flow speed and direction of MTCs as shown in **Supplementary Fig. 9**.

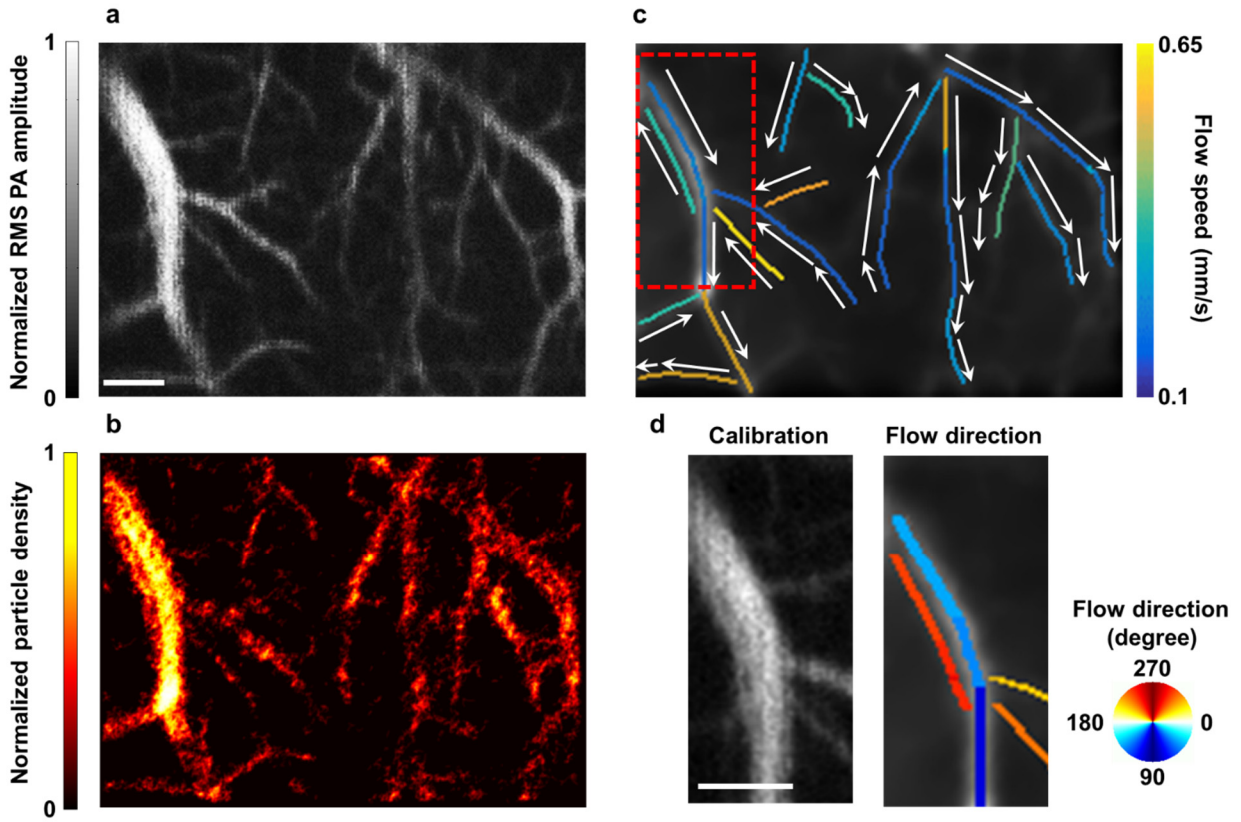

Supplementary Figure 9. Localization and tracking of MTCs in the mouse brain. (a) Calibration image of the cortical region through an intact skull. (b) Localization map reconstructed by superimposing the tracked MTC positions from all frames. (c) Velocity-contrast map for the mouse

cortical vasculatures computed by analyzing the flow speed of MTCs in each vessel in the spatiotemporal frequency domain. The arrows indicate the flow directions of the MTCs. (d) Flow direction map of the MTCs from the boxed region in (c) compared to the calibration image. All scale bars, 500 μm.

Supplementary Note 3. Order-of-magnitude estimation of the total number of resolvable pixels in the reconstructed image of PATER.

We first consider the information in the unit of bits in an image containing N_p pixels:

$$N_p b_p, \tag{21}$$

where b_p is the bit depth desired for each pixel's digitized signal.

In widefield mode, the detected signal $u(t)$ has a time duration of T_w. The temporal resolution Δt of the detected time course is determined by the high cutoff frequency f_{HC} of the signal:

$$\Delta t = \frac{1}{2f_{HC}}. \tag{22}$$

Thus, the information capacity of the widefield signal detected by PATER is estimated to be

$$\frac{T_w}{\Delta t} \cdot \mathrm{b_w} = 2f_{HC}T_w \cdot b_w, \tag{23}$$

where b_w is the bit depth used to digitize $u(t)$. To well reconstruct the widefield image using PATER, the following condition must be satisfied:

$$N_p b_p \leq 2f_{HC}T_w \cdot b_w. \tag{24}$$

In our current experimental settings, $T_w = 164$ μs, $f_{HC} = 25$ MHz, and $b_w = 12$. In calibration mode, we have achieved an SNR = 70; thus, we desire $b_p \approx \log_2 70 \approx 7$. Therefore, from Eq. (24), the maximum number of resolvable pixels N_p is approximately 14,000.

Supplementary Note 4. Comparison of SNRs between point and widefield illuminations in PATER.

We consider a widefield image containing N_p resolvable pixels. Calibration yields N_p unit-norm calibration vectors $\hat{e}_1, \hat{e}_2, \dots, \hat{e}_{N_p}$, each representing a normalized time-resolved PA signal from a single pixel. For simplicity, we assume that they are noise-free and orthogonal to each other (i.e., $\hat{e}_i \cdot \hat{e}_j = 0$, if $i \neq j$, and $i, j = 1,2, \dots, N_p$).

In widefield mode, the detected signal $\vec{e}$ can be expressed as

$$\vec{e} = \sum_1^{N_p} \mu_i \hat{e}_i + \vec{n}, \tag{25}$$

where μ_i denotes the true RMS signal amplitude of the i^{th} pixel and $\vec{n}$ denotes the noise vector. PATER's image reconstruction is equivalent to vector projection to each pixel's basis vector—which may also be considered matched filtering:

$$\vec{e} \cdot \hat{e}_i = \mu_i + n_i. \tag{26}$$

While the first term on the right side represents the true pixel value in RMS signal amplitude, the second term represents the projected RMS noise amplitude $n_i = \vec{n} \cdot \hat{e}_i$. The expected SNR can be expressed as

$$SNR_{wf} = \frac{\mu_i}{\langle |n_i| \rangle}. \tag{27}$$

For a fair comparison, the light fluence (mJ/cm^2) is kept identical for both widefield and point-scanning measurements. For point-scanning imaging without calibration data, the signal $\vec{e}$ for the i^{th} pixel can nevertheless be expressed as

$$\vec{e} = \mu_i \hat{e}_i + \vec{n}. \tag{28}$$

In photoacoustics, noise mainly arises from three sources: thermal acoustic noise from the medium, thermal noise from the ultrasonic transducer, and electronic noise from the amplifier[2, 3]. Independent of light illumination, $\vec{n}$ is statistically identical for both widefield and point-scanning measurements.

Without knowledge of $\hat{e}_i$ during the experiment in this mode, we use the RMS value of $\vec{e}$ (i.e., the norm $\|\vec{e}\|$) instead as the measured pixel value:

$$\|\vec{e}\| = \sqrt{\mu_i^2 + n^2 + 2\mu_i \hat{e}_i \cdot \vec{n}}, \tag{29}$$

which is approximately equal to μ_i if $n \ll \mu_i$ ($n = \|\vec{n}\|$). The RMS noise relative to the true value of μ_i can be estimated as follows:

$$noise_{sp} = |\|\vec{e}\| - \mu_i| = \left|\sqrt{\mu_i^2 + n^2 + 2\mu_i \hat{e}_i \cdot \vec{n}} - \mu_i\right|. \tag{29}$$

As $n \ll \mu_i$, Eq. (30) can be approximated to

$$noise_{sp} = |n_i|. \tag{30}$$

Therefore, the point-scanning pixel SNR is

$$SNR_{sp} = \frac{\mu_i}{\langle |n_i| \rangle}, \tag{31}$$

which approximately equals the widefield SNR for the same pixel as long as $n \ll \mu_i$ holds true. This conclusion has also been experimentally validated.

Supplementary Video 1. Demonstration of PATER's imaging mechanism. The acoustic ergodic relay encodes the PA signals as they propagate from the source to the detector. In the calibration mode, the point-by-point encoded responses are recorded. In the widefield mode, the detected signals are decoded by the reconstruction algorithm using the calibrated impulse responses. The resulting images are then displayed. The propagations of PA signals inside the ergodic relay are simulated using the *k*-wave toolbox.

Supplementary Video 2. Quantification of the spatial resolution of snapshot widefield imaging by PATER. After calibration, two 30-μm-diameter light beams were shone on a black sheet. While one beam was held stationary in the centre, the other beam was translated linearly away from the first. The step size was 15 μm, and the FOV was 1.5×0.75 mm^2.

Supplementary Video 3. Snapshot widefield imaging by PATER of blood flow behind biological tissue. A tissue phantom consisting of two tubes with blood placed behind a layer of chicken breast tissue was imaged. Tube 1 without flow served as the control while Tube 2 with blood being flushed out was monitored. The video with an original recording frame rate of 2 kHz was down-sampled 200× to a playback rate of 10 Hz.

Supplementary Video 4. Snapshot widefield functional PATER imaging of haemoglobin responses in a mouse brain to front-paw stimulations *in vivo*. An 8×6 mm^2 FOV of the mouse cortex was monitored at a frame rate of 10 Hz. The fractional changes in PA signal amplitude (shown in red) in response to right- and left-paw stimulations were superimposed on the calibration

image (shown in grey). The average change in the PA signal amplitude in the somatosensory region over time, peaking at ~6.4%, was plotted at the bottom of the video.

Supplementary Video 5. Visualization of blood pulse wave propagation in the middle cerebral arteries. A 3 × 3 mm^2 FOV of the mouse cerebral region was imaged at a frame rate of 2 kHz. Five heating cycles were displayed.

Supplementary Video 6. Snapshot widefield tracking of MTCs in a tube using PATER at 660 nm light illumination. A tube (0.1 mm inner diameter) filled with blood was first imaged in calibration mode. An MTC cluster mixed with blood was then injected at a speed of 1 mm/s. The migration of the MTCs through the tube was monitored with widefield measurements. The video with an original recording frame rate of 1 kHz is down-sampled 20× to a playback rate of 50 Hz.

Supplementary Video 7. Snapshot widefield tracking of MTCs in a mouse brain *in vivo* using PATER at 660 nm light illumination. A 2 × 2 mm^2 FOV of the mouse cortical region was monitored at a frame rate of 2 kHz for 100 seconds. The video was down-sampled 200× to a playback rate of 10 Hz.

Supplementary Video 8. Close-up slow-motion video of snapshot widefield tracking of MTCs as shown in Supplementary Video 6.

Supplementary Video 9. Buildup of MTC localization map. The positions of migrating MTCs in the blood vessels were tracked throughout the video from Supplementary Video 6 and superimposed.

References

1. Srinivasan VJ, Sakadžić S, Gorczynska I, Ruvinskaya S, Wu W, Fujimoto JG*, et al.* Quantitative cerebral blood flow with optical coherence tomography. *Optics express* 2010, **18**(3)**:** 2477-2494.

2. Winkler AM, Maslov K, Wang LV. Noise-equivalent sensitivity of photoacoustics. *Journal of Biomedical Optics* 2013, **18**(9)**:** 097003.

3. Yao J, Wang LV. Sensitivity of photoacoustic microscopy. *Photoacoustics* 2014, **2**(2)**:** 87-101.